



## NRC Publications Archive Archives des publications du CNRC

### **Mechanism-based modeling for low cycle fatigue of cast austenitic steel**

Wu, Xijia; Quan, Guangchun; Sloss, Clayton

This publication could be one of several versions: author's original, accepted manuscript or the publisher's version. / La version de cette publication peut être l'une des suivantes : la version prépublication de l'auteur, la version acceptée du manuscrit ou la version de l'éditeur.

For the publisher's version, please access the DOI link below. / Pour consulter la version de l'éditeur, utilisez le lien DOI ci-dessous.

#### **Publisher's version / Version de l'éditeur:**

<https://doi.org/10.1007/s11661-017-4160-4>

*Metallurgical and Materials Transactions A*, 48, 9, pp. 4058-4071, 2017-06-07

#### **NRC Publications Record / Notice d'Archives des publications de CNRC:**

<https://nrc-publications.canada.ca/eng/view/object/?id=385f34ee-c572-427c-832e-666b43a79f08>

<https://publications-cnrc.canada.ca/fra/voir/objet/?id=385f34ee-c572-427c-832e-666b43a79f08>

Access and use of this website and the material on it are subject to the Terms and Conditions set forth at

<https://nrc-publications.canada.ca/eng/copyright>

READ THESE TERMS AND CONDITIONS CAREFULLY BEFORE USING THIS WEBSITE.

L'accès à ce site Web et l'utilisation de son contenu sont assujettis aux conditions présentées dans le site

<https://publications-cnrc.canada.ca/fra/droits>

LISEZ CES CONDITIONS ATTENTIVEMENT AVANT D'UTILISER CE SITE WEB.

**Questions?** Contact the NRC Publications Archive team at

PublicationsArchive-ArchivesPublications@nrc-cnrc.gc.ca. If you wish to email the authors directly, please see the first page of the publication for their contact information.

**Vous avez des questions?** Nous pouvons vous aider. Pour communiquer directement avec un auteur, consultez la première page de la revue dans laquelle son article a été publié afin de trouver ses coordonnées. Si vous n'arrivez pas à les repérer, communiquez avec nous à PublicationsArchive-ArchivesPublications@nrc-cnrc.gc.ca.



# Mechanism-Based Modeling for Low Cycle Fatigue of Cast Austenitic Steel



XIJIA WU, GUANGCHUN QUAN, and CLAYTON SLOSS

A mechanism-based approach—the integrated creep-fatigue theory (ICFT)—is used to model low cycle fatigue behavior of 1.4848 cast austenitic steel over the temperature range from room temperature (RT) to 1173 K (900 °C) and the strain rate range from  $2 \times 10^{-4}$  to  $2 \times 10^{-2} \text{ s}^{-1}$ . The ICFT formulates the material's constitutive equation based on the physical strain decomposition into mechanism strains, and the associated damage accumulation consisting of crack nucleation and propagation in coalescence with internally distributed damage. At room temperature, the material behavior is controlled by plasticity, resulting in a rate-independent and cyclically stable behavior. The material exhibits significant cyclic hardening at intermediate temperatures, 673 K to 873 K (400 °C to 600 °C), with negative strain rate sensitivity, due to dynamic strain aging. At high temperatures  $>1073 \text{ K}$  (800 °C), time-dependent deformation is manifested with positive rate sensitivity as commonly seen in metallic materials at high temperature. The ICFT quantitatively delineates the contribution of each mechanism in damage accumulation, and predicts the fatigue life as a result of synergistic interaction of the above identified mechanisms. The model descriptions agree well with the experimental and fractographic observations.

DOI: 10.1007/s11661-017-4160-4

© Published with permission of the Crown in Right of Canada 2017

## I. INTRODUCTION

AUSTENITIC stainless steels are widely used to cast hot-end components of exhaust systems of internal combustion engines (ICE), especially when the gas temperature reaches above 900 °C. Under such severe operating conditions, low cycle fatigue (LCF) and thermomechanical fatigue (TMF) are inevitably the major failure modes concerned in the component design. Life prediction for LCF and TMF of austenitic stainless steels is particularly challenging, because the damage process involves multiple deformation mechanisms such as plasticity, dynamic strain aging (DSA) from solute drag effect,<sup>[1]</sup> and creep, which result in a cyclically non-stable behavior in combination with oxidation.<sup>[2–4]</sup> Many conventional fatigue analysis methods have been proposed such as strain-based Coffin–Manson relation<sup>[5]</sup> and energy-based Morrow equation,<sup>[6]</sup> but they do not delineate these mechanisms explicitly.

In order to delineate the contributions of material-intrinsic (deformation mechanisms) and extrinsic (environmental effects) factors in LCF and TMF, it is advantageous to use mechanism-based constitutive laws to evaluate the mechanism strain responsible for the respective damage, instead of the lump-sum viscoplastic strain obtained with the unified constitutive theory.<sup>[7]</sup> The reason is the following, as commonly understood by physical metallurgy: fatigue damage is caused by alternating plasticity *via* irreversible slip *via* dislocation glide<sup>[8–11]</sup>; while creep by dislocation climb *via* vacancy flow releases dislocations piled-up at obstacles in glide,<sup>[12,13]</sup> which tends to ease the fatigue damage; and on the other hand, vacancy flow and grain boundary sliding promotes cavitation and void growth along grain boundaries,<sup>[14,15]</sup> which lead to the formation of internally distributed damage. These different mechanisms result in either transgranular or intergranular failure. Apparently, the unified viscoplastic strain is not suitable for correlation with failure modes since multiple failure modes may occur with a single-value inelastic strain, depending on whether it is accumulated by plasticity or creep. The ICFT has been successfully applied to ductile cast iron for the above purposes.<sup>[16,17]</sup>

In this study, the mechanism-based approach—ICFT—is used to analyze the cyclic behavior of 1.4848 cast austenitic steel. LCF experiments were conducted on this alloy at different strain rates from  $2 \times 10^{-4}$  to  $2 \times 10^{-2} \text{ s}^{-1}$  in the temperature range from room

---

XIJIA WU is with the National Research Council Canada, Ottawa, ON, K1A 0R6, Canada. Contact e-mail: Xijia.Wu@nrc-cnrc.gc.ca  
GUANGCHUN QUAN is with Wecast Industries Inc., Savannah Oaks Dr., Brantford, ON, N3T 5V7, Canada, and also with Tenneco Automotive Operating Company Inc., 3901 Willis Rd, Grass Lake, MI, 49240. CLAYTON SLOSS is with Wecast Industries Inc.

Manuscript submitted December 12, 2016.

temperature (RT) to 1173 K (900 °C). The deformation and damage mechanisms involved are discussed in relation to the observed behavior. Life of LCF is evaluated with consideration of mechanical fatigue, environmental effects, and interactions with internally distributed damage as induced by DSA at intermediate temperatures and creep at high temperatures.

## II. EXPERIMENTAL

The austenitic cast stainless steel used in this study was 1.4848 with the nominal chemical composition as given in Table I. Strain-controlled LCF tests were conducted on a MTS uniaxial servo hydraulic test frame, model MTS 810 equipped with an ATS series 3210 three-zone radiation furnace. During the test, the temperature was controlled using 3 K-type thermocouples with fixed mounting positions within the furnace hot zone. Closed loop control of the specimen loading was achieved by measuring the elongation of the specimen with an MTS model 632.54 extensometer and using an MTS model GT493 digital controller regulating the force applied to the specimen. The load applied to the specimen was monitored with an MTS Model 661 load cell.

Fatigue testing was conducted, following the ASTM Standard E606-04, at strain rates of 0.02, 0.002, and 0.0002 s<sup>-1</sup> in the temperature range of RT to 1173 K (20 °C to 900 °C). Post-mortem fractographic examination of the fracture surfaces was conducted using a Philips XL30S scanning electron microscope (SEM).

## III. MECHANISM-BASED CONSTITUTIVE EQUATIONS

It has been recognized that metallic materials can change shape by plastic deformation, creep, and diffusion.<sup>[13]</sup> Figure 1 shows a schematic of deformation mechanism map. Generally, rate-independent plasticity occurs by dislocation glide and cross slip at low temperatures (*i.e.*,  $T < 0.3T_m$ , where  $T_m$  is the melting temperature in Kelvin). In this regime, dislocations can pile up at obstacles such as precipitates and inclusions, resulting in strain hardening. Under cyclic loading, alternating dislocation glide results in crystallographic slip and slip reversal, leading to fatigue. As temperature increases, some pile-up dislocations can climb along the obstacles and continue to glide, when assisted by vacancy diffusion, such that time-dependent deformation, *i.e.*, creep, is manifested. Creep deformation at elevated temperatures occurs *via* dislocation climb and glide: (i) along grain boundaries, resulting in grain boundary sliding (GBS); and (ii) within the grain interior, resulting in intragranular deformation (ID).

Pure diffusional flow may occur in metals at low stresses and high temperatures, but it is often neglected in engineering alloys.

In previous work, a framework of integrated creep-fatigue theory has been outlined and applied to Co-base/Ni-base superalloys and ductile cast iron,<sup>[16–19]</sup> where the total deformation comprises elastic-plastic deformation and creep,

$$\varepsilon = \left( \frac{\sigma}{E} + \varepsilon_p \right) + \varepsilon_v, \quad [1]$$

where  $\sigma$  is the normal stress;  $E$  is the Young's modulus;  $\varepsilon_p$  is plastic strain; and  $\varepsilon_v$  is creep strain. Here, the deformation quantities within the bracket are instantaneous and rate-independent. The creep strain  $\varepsilon_v$  is time-dependent, and it can be further decomposed into mechanism-based strains such as ID, GBS, and diffusion.

Rate-independent plasticity is often described by

$$\varepsilon_p = \left( \frac{\sigma - \sigma_0}{K} \right)^n, \quad [2]$$

where  $\sigma_0$  represents the initial yield stress, while  $K$  is the plastic drag stress and  $n$  is the stress exponent. Here, it should be noted that the classical theory of plasticity has been robustly implemented in commercial finite element method (FEM) software packages such as Abaqus and MSC.Marc, such that either Eq. [2] or tabulated tensile data can be input to perform incremental plasticity analysis with options of kinematic and/or isotropic hardening. In this study, Eq. [2] is merely used to analyze the uniaxial tensile behavior of rate-independent plasticity. Once the mechanism-based parameters are determined, the constitutive equation(s) can be implemented into the appropriate subroutine(s) of

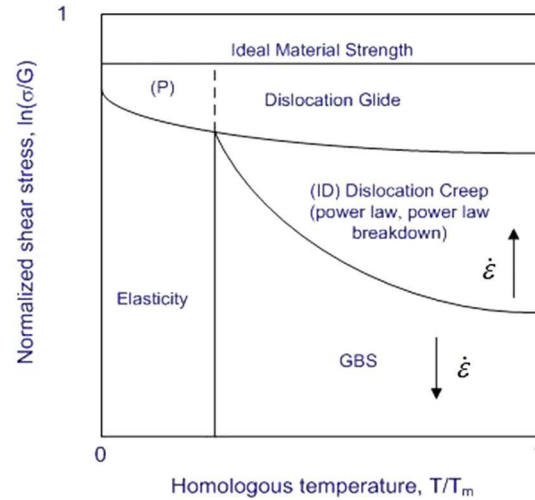


Fig. 1—Schematic of deformation mechanism map.

Table I. Composition of 1.4848 Austenitic Steel (Wt. Percent)

C	Si	Mn	Ni	Cr	Fe
0.35	1.5	0.6	20	25	bal.

commercial FEM for 3D analysis. The same principle is true for creep discussed in the following.

As mentioned earlier, creep occurs by a plethora of mechanisms including intragranular dislocation glide plus climb as well as GBS. During strain-controlled tensile loading, it is always the fastest mechanism that causes material yielding. According to the deformation mechanism maps,<sup>[13]</sup> as shown in Figure 1, dislocation glide tends to dominate in the high stress region, resulting in the flow stress behavior after yielding. The stress-dependency of dislocation glide can be described by many functions such as power-law, hyperbolic sine, and hyperbolic sine to the power of  $n$ . Actually, it has been shown that within the strain rate range of  $10^{-8}$  to  $10^0 \text{ s}^{-1}$ , all the above functions are equivalent for the same rate phenomenon.<sup>[7]</sup> Therefore, without losing generality, here we use the rate equation for single-barrier-activation to represent the thermally activated dislocation glide plus climb,<sup>[20]</sup> which has a hyperbolic sine form, as

$$\dot{\epsilon}_v = 2A \sinh\left(\frac{V(\sigma - \sigma_b)}{kT}\right), \quad [3a]$$

where

$$A = A_0 \exp\left(-\frac{Q}{RT}\right), \quad [3b]$$

where  $A_0$  is the pre-exponential rate constant,  $Q$  is the activation energy,  $V$  is the activation volume,  $\sigma_b$  is the back stress,  $k$  is the Boltzmann constant,  $R$  is the universal gas constant, and  $T$  is the absolute temperature.

In the following, we will derive the back stress from the dislocation pile-up and release mechanism as schematically shown in Figure 2. In keeping consistency with the driving force for plastic deformation, we use the shear stress and strain terms,  $\tau$  and  $\gamma$ . Under uniaxial loading conditions, the uniaxial normal stress and strain are related to the shear stress and strain by the Taylor's factor:  $\sigma = \sqrt{3}\tau$  and  $\epsilon = \gamma/\sqrt{3}$ . As plastic deformation proceeds, the gliding dislocations may be obstructed by obstacles as shown in Figure 2. The stress field of these dislocations acts as a back stress on mobile dislocations. Suppose that the distance between the dislocation source (e.g., a Frank–Reed source) and the obstacle is  $\lambda$ , and there are  $n$  dislocations in the pile-up at time  $t$ . The back stress that pile-up dislocations together exert on a moving dislocation located at a distance  $x$  away is equal to  $n$  times the stress by unit dislocation<sup>[21]</sup>

$$\tau_i(x) = \frac{nGb}{2\pi(1-\nu)x}, \quad [4]$$

where  $\nu$  is the Poisson's ratio,  $G$  is the shear modulus, and  $b$  is the Burgers vector.

The average back stress opposing dislocation glide,  $\tau_b$ , can be defined as the mechanical work against the dislocation glide over the distance  $\lambda$ , as

$$\tau_b = \frac{1}{\lambda} \int_{\lambda}^{\lambda} \tau_i(x) dx. \quad [5]$$

Substituting Eq. [4] into Eq. [5], the integration leads to

$$\tau_b = \frac{nGb}{2\pi(1-\nu)\lambda} \ln \frac{\lambda}{nb}. \quad [6]$$

The number of dislocations arriving per unit time is given by  $\rho vs$ , where  $\rho$  is the dislocation density,  $v$  is the dislocation velocity, and  $s$  is the slip-band width. At the same time, the number of dislocations leaving the pile-up is equal to  $n\kappa$ , where  $\kappa$  is the rate of climb. Hence, for a single slip system, the change in the number of pile-up dislocations in a unit time is given by

$$\frac{dn}{dt} = \rho vs - \kappa n. \quad [7]$$

By the Orowan equation,  $\dot{\gamma} = \rho bv$  ( $s \approx b$ ), Eq. [7] becomes

$$\frac{dn}{dt} = \dot{\gamma} - \kappa n. \quad [8]$$

Differentiating Eq. [6] with respect to time, and substituting Eq. [8] into the differential equation,

$$\dot{\tau}_b = \frac{Gb}{2\pi(1-\nu)\lambda} \left[ \ln\left(\frac{\lambda}{nb}\right) - 1 \right] (\dot{\gamma} - n\kappa). \quad [9]$$

Consider that usually  $\ln(\lambda/nb) \gg 1$ , Eq. [9] can be simplified as

$$\dot{\tau}_b = H\dot{\gamma} - \kappa\tau_b, \quad [10]$$

where  $H = [Gb/2\pi(1-\nu)\lambda]\ln(\lambda/nb)$  is the work-hardening coefficient, which can be practically considered as a microstructure constant, since the logarithmic variation with  $n$  is usually small when  $n$  is large. Equation [10] formulates the strain hardening-recovery mechanism with the first term  $H\dot{\gamma}$  representing work hardening arising from dislocation glide, and the second term  $\tau_b\kappa$  representing recovery as controlled by dislocation climb.

According to the deformation kinetics,<sup>[22]</sup> it is always the highest rate mechanism that dominates when multiple mechanisms operate independently. Under

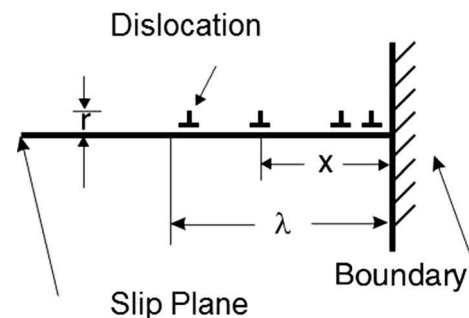


Fig. 2—A schematic of dislocation pile-up against an obstacle.

strain-controlled loading conditions, deformation is forced to keep up with the loading rate, and hence the highest rate mechanism prevails to yield the plastic flow. Particularly, at high strain rates representative of engine start-up and shutdown, deformation is controlled by rate-independent plasticity in combination with thermally activated dislocation glide; other low-stress operating mechanisms can be quickly passed at such high loading rate.

Under uniaxial constant-strain-rate deformation conditions, according to Eq. [1], the material behavior obeys the deformation constraint

$$\dot{\epsilon} = \frac{\dot{\sigma}}{E} + \dot{\epsilon}_p + \dot{\epsilon}_v = \text{constant}. \quad [11]$$

Under more general loading conditions, especially in 3D components, the stress-strain response would be played out by the mechanism-based constitutive equation subjected to the boundary conditions of the component. Therefore, the following analysis is a case study of the ICFT for uniaxial deformation.

Under isothermal LCF conditions, the rate of plastic strain  $\epsilon_p$  accumulation, according to Eq. [2], can be expressed as

$$\dot{\epsilon}_p = \frac{n}{K} \left( \frac{\sigma - \sigma_0}{K} \right)^{n-1} \dot{\sigma}. \quad [12]$$

Equation [12] is in accordance with the incremental flow theory of plasticity.<sup>[23]</sup> Here, the expression is provided for monotonic loading though, when implemented in the plasticity subroutine of commercial FEM software, as mentioned before, incremental plastic deformation will be automatically evaluated by FEM that embodies the classical theory of plasticity. This has been demonstrated in an earlier study for ductile cast iron.<sup>[16,17]</sup>

Substituting Eq. [12] into Eq. [11], we have

$$\dot{\epsilon} = \frac{\dot{\sigma}}{E} + \dot{\epsilon}_p + \dot{\epsilon}_v = \left( 1 + \frac{nE}{K} \left( \frac{\sigma - \sigma_0}{K} \right)^{n-1} \right) \frac{\dot{\sigma}}{E} + \dot{\epsilon}_v. \quad [13]$$

We define the plasticity-accommodated tangent modulus as

$$\frac{1}{E_t} = \left( \frac{1}{E} + \frac{n}{K} \left( \frac{\sigma - \sigma_0}{K} \right)^{n-1} \right). \quad [14]$$

Then, Eq. [13] can be rewritten as

$$\dot{\epsilon} = \frac{\dot{\sigma}}{E_t} + \dot{\epsilon}_v. \quad [15]$$

Under fast strain rate loading, we assume  $H\dot{\gamma} \gg \tau_b \kappa$ , in Eq. [10]. Then, converting to the normal strain under uniaxial loading,  $\dot{\sigma}_b \approx H\dot{\epsilon}_v$  (in the present study, at high temperatures when time-dependent deformation arises, linear work hardening is indeed observed, which will be discussed later, and henceforth the work-hardening

coefficient is determined in the *normal* sense), Eq. [3] can be rewritten as

$$\dot{\epsilon}_v = 2A \sinh \Psi, \quad [16a]$$

where

$$\dot{\Psi} = \frac{V}{kT} (\dot{\sigma} - H\dot{\epsilon}_v). \quad [16b]$$

Here,  $\Psi$  is defined as the ratio of mechanical energy to thermal energy of the activation system.

Combining Eqs. [15] and [16], we have the governing differential equation for  $\Psi$ , as

$$\dot{\Psi} = \frac{E_t V}{kT} \left[ \dot{\epsilon} - 2A \left( 1 + \frac{H}{E_t} \right) \sinh \Psi \right]. \quad [17]$$

This differential equation can be solved in infinitesimal steps as follows. We assume that the evolution of the energy,  $\Psi$ , undergoes a series of infinitesimally small increments, for each  $i$ -th step, the energy state evolves from  $\Psi_{i-1}$  to  $\Psi_i$  over the time interval  $\Delta t_i = t_i - t_{i-1}$ . Within this interval, the stress and transient tangent  $E_t$  are constant. Then, following the solution procedures of Reference 20, we have

$$\ln \left( \frac{e^{-\Psi} - a}{\chi e^{-\Psi} + b} \right) \Big|_{\Psi_{i-1}}^{\Psi_i} = - \frac{VE_t \dot{\epsilon} \sqrt{1 + \chi^2}}{kT_i} \Delta t_i \quad (i = 1, 2, \dots). \quad [18]$$

Summing up all these infinitesimal steps, we have

$$\sum_{i=1}^N \ln \left( \frac{e^{-\Psi} - a}{\chi e^{-\Psi} + b} \right) \Big|_{\Psi_{i-1}}^{\Psi_i} = - \sum_{i=1}^N \frac{VE_t \dot{\epsilon} \sqrt{1 + \chi^2}}{kT_i} \Delta t_i, \quad [19a]$$

where

$$\chi = \frac{2A}{\dot{\epsilon}} \left( 1 + \frac{H}{E} \right), \quad a = \frac{\sqrt{1 + \chi^2} - 1}{\chi}, \quad b = \sqrt{1 + \chi^2} + 1. \quad [19b]$$

Let  $N \rightarrow \infty$ , the left-hand side of Eq. [19a] will be equal to the logarithmic difference between the final state and the initial state, since the intermediate steps are all canceled out, and the right-hand side is integration over the loading period. After mathematical rearrangement, we have

$$\left( \frac{e^{-\Psi} - a}{\chi e^{-\Psi} + b} \right) = \left( \frac{1 - a}{\chi + b} \right) \exp \left\{ - \int_{t_0}^t \frac{VE_t \dot{\gamma} \sqrt{1 + \chi^2}}{kT} dt \right\}, \quad [20]$$

where  $t_0$  is the time to reach the elastic limit, or in other words, when plastic flow commences.

The elastic limit  $\sigma_0$  is defined by

$$\Psi_0 = \frac{(\sigma - \sigma_0)}{kT} = 0. \quad [21]$$

From Eq. [20], we can obtain the stress–strain response as follows:

$$\sigma - H\varepsilon_v - \sigma_0 = -\frac{kT}{V} \ln\left(\frac{a + \omega b}{1 - \omega\chi}\right), \quad [22a]$$

where  $\omega$  is the response function defined by

$$\omega(\varepsilon) = \left(\frac{1-a}{\chi+b}\right) \exp\left\{-\frac{V \int_{\varepsilon_0}^{\varepsilon} E_t \sqrt{1+\chi^2} d\varepsilon}{kT}\right\}, \quad [22b]$$

where  $\varepsilon_0 = \sigma_0/E$ .

The above model has seven (7) material parameters ( $K$ ,  $n$ ,  $\sigma_0$ ,  $A_0$ ,  $Q$ ,  $V$ , and  $H$ ) in total. They are defined with respect to the physical mechanisms involved, and their roles in governing the stress–strain relationship are explicitly expressed as in the analytical form, Eq. [22]. For rate-independent plasticity,  $\sigma_0$  represents the minimum lattice resistance,  $K$  represents the drag stress responsible for isotropic hardening, and  $n$  is the power exponent. These can all be temperature-dependent, as usually the case. The activation parameters,  $A_0$ ,  $Q$ ,  $V$ , are assumed to be constants for an ideal constant structure. The work-hardening coefficient  $H$  is also temperature-dependent, as it is proportional to the shear modulus  $G$ . For 3D component analysis, the validated uniaxial model can be implemented into FEM in two parts: (1) (rate-independent) plasticity and (2) creep, through either existing or user subroutines, but run with both at the same time, as seen in, *e.g.*, Reference 24.

The present model will reduce to rate-independent plasticity when the time-dependent mechanisms do not operate (*e.g.*, when  $\dot{\varepsilon}_v \approx 0$  at low temperature). When thermally activated processes intervene, the stress–strain response will show rate-dependence. In describing the cyclic behavior of a material, if the material is cyclically stable, Eq. [22] can be used to describe the cyclic stress–strain curve, as in the case for DCI.<sup>[16,17]</sup> If the material is not cyclically stable, the cyclic stress–strain relation needs to be tracked with an additional internal state variable for either cyclic hardening or softening. However, for practical reasons, it is more advantageous to choose a cyclically stable quantity for LCF life correlation. In this regard, the plastic energy may be an appropriate parameter.<sup>[6,25]</sup> In the following section, the cyclic deformation behaviors of 1.4848 austenitic cast steel are discussed along with the model descriptions using the mechanism-based deformation formulation, in the context of Eqs. [1] through [22].

## IV. RESULTS AND DISCUSSION

### A. Cyclic Behavior

#### 1. Room-temperature behavior

The room temperature (RT) hysteresis behaviors of cast austenitic stainless steel 1.4848 at strain rate of  $\dot{\varepsilon} = 0.02 \text{ s}^{-1}$  are shown in Figure 3, which appear to be cyclically stable for the majority of its life cycles at all strain amplitudes. When the hysteresis loops are displaced with the zero points setting at the maximum

compression states as shown in Figure 4 (the hysteresis loop of 1 pct strain range at  $\dot{\varepsilon} = 0.002 \text{ s}^{-1}$  is also shown for comparison), one finds that the material exhibits a Masing behavior at room temperature. For stabilized Masing behavior, both the hysteresis loops and the cyclic stress–strain relationship can be described by Eq. [2], which has been a standard practice in fatigue analysis. The Masing behavior is apparently attributed to rate-independent plasticity, when all the other rate-dependent mechanisms are absent (negligible) at room temperature.

#### 2. Intermediate temperature behavior [673 K to 873 K (400 °C to 600 °C)]

As observed at 673 K (400 °C), the material's cyclic behavior exhibited significant cyclic hardening until fracture, especially at a slow strain rate,  $\dot{\varepsilon} = 0.002 \text{ s}^{-1}$ , as shown in Figure 5. Dynamic strain aging (DSA) has been known to contribute to cyclic hardening of austenitic stainless steels such as type 316L austenitic stainless steel in the temperature range of 523 K to 823 K (250 °C to 550 °C).<sup>[2,3]</sup> DSA is a result of interaction between diffusing solute atoms and mobile dislocations during plastic deformation. It is manifested by pinning of slow moving dislocations, restricting the cross slip of screw dislocations, and hence enhancing slip inhomogeneity, thus resulting in an increased stress (hardening) to reach the prescribed strain level. In a cyclic process, this means continued evolution of the hysteresis loops with the number of cycles. The behavior (Figure 5) poses a significant challenge to stress modelers in that every hysteresis loop has to be computed until the final cycle to failure. Here, we shall try a simulation case for cyclic deformation at 673 K (400 °C) as follows.

Figure 6 shows the experimental hysteresis loops recorded from the 1st cycle to 4134th cycle (near to failure), cycling between  $\pm 0.34$  pct strain at  $\dot{\varepsilon} = 0.002 \text{ s}^{-1}$ . The material experienced continuous cyclic hardening due to the DSA effect. To account for that effect, we modify Chaboche's internal state variable  $R$  formulation,<sup>[7]</sup> as

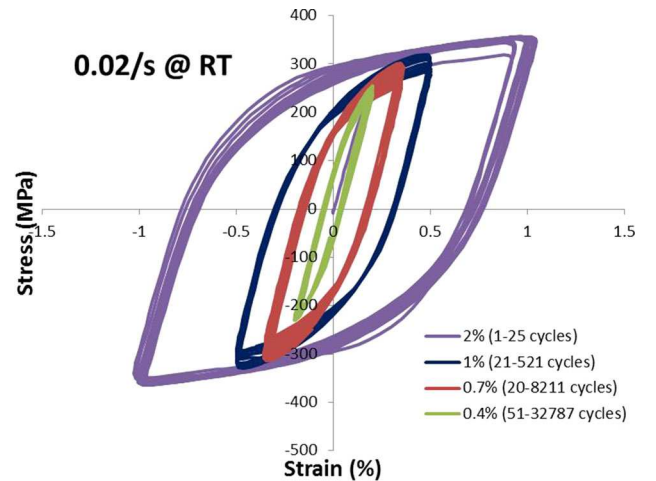


Fig. 3—Hysteresis loops of cast austenitic steel at RT.

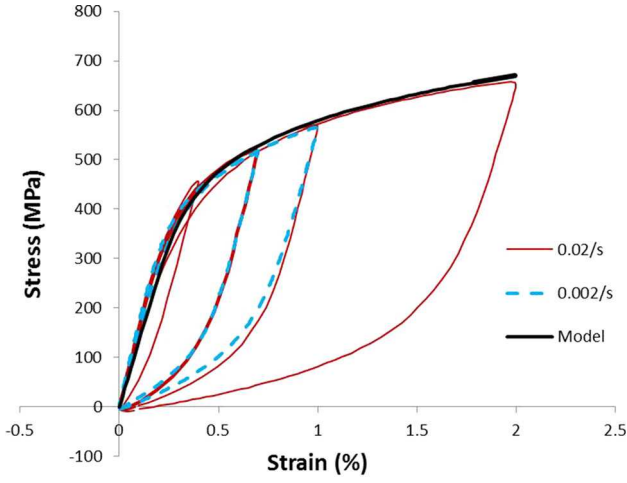


Fig. 4—Stabilized hysteresis loops of austenitic cast steel at room temperature.

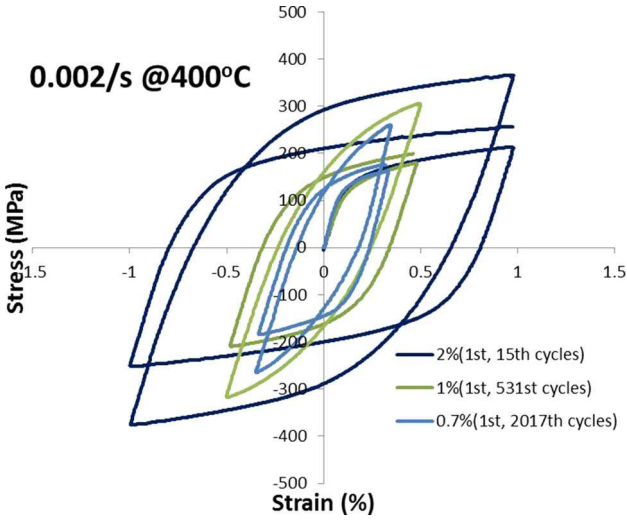


Fig. 5—Hysteresis loops of cast austenitic steel at 673 K (400 °C).

$$\dot{R} = [b(Q - R + cp) + c]\dot{p}, \quad [23]$$

where  $b$ ,  $Q$ ,  $c$  are material constants and  $p$  is the accumulated plastic strain. Here, a new term  $cp$  is introduced to describe the steady increase of isotropic hardening (in Chaboche's original formulation,  $c = 0$ , and therefore it describes isotropic hardening approaching a constant level). The integration of Eq. [23] lead to

$$R = Q[1 - \exp(-bp)] + cp. \quad [24]$$

And it adds to the drag stress as  $K = K_0 + R$ , with  $K_0$  being the drag stress (denominator of the applied stress in Eq. [2]) in absence of isotropic hardening.

As cyclic plastic strain accumulates under DSA conditions, dislocation structure would evolve, which also leads to change in the power-law exponent,  $n$ . By the same token, we formulate  $n$  as

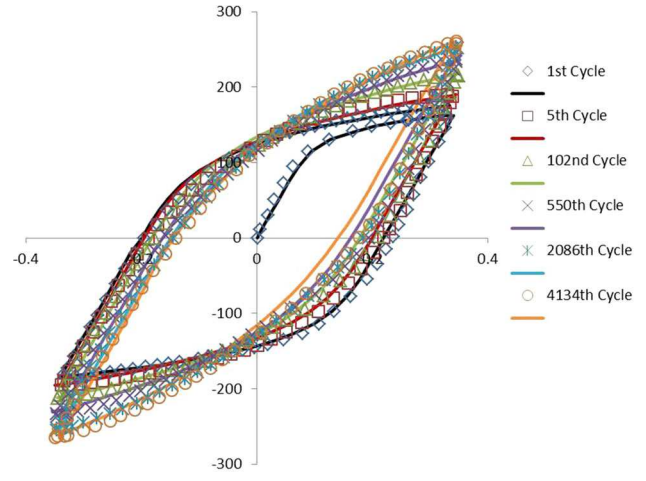


Fig. 6—Experimental and simulated hysteresis loops of cast austenitic steel cycled between  $\pm 0.34$  pct strain at strain rate of  $0.002 \text{ s}^{-1}$ , 673 K (400 °C).

$$n = n_0 - Q_n[1 - \exp(-b_n p)] + c_n p, \quad [25]$$

where  $b_n$ ,  $Q_n$ ,  $c_n$ , and  $n_0$  are material constants.

With the above two equations to describe the evolution of plasticity constants  $K$  and  $n$  under DSA condition as shown in Figure 7 for the best-fit, and a constant kinematic hardening for each reversal, the hysteresis loops can be simulated, as shown in Figure 6 (lines). Equations [24] and [25] may be of phenomenological interest per cyclic test condition, but it will be very tedious to be implemented for component analysis, for which hundreds or even thousands of material finite elements must be updated cycle by cycle until final failure at thousands or millions of cycles. Therefore, in the following analysis, we seek some simplified representation of the DSA-affected behavior in terms of cyclic stress–strain curves.

Solute drag and dislocation-solute dynamic models have been developed to describe the DSA-induced serrated flow in terms of dislocation density or dislocation velocity.<sup>[21,26]</sup> Miller pointed out that DSA contributes to the drag stress for viscoplasticity, based on the Cottrell mechanism.<sup>[27]</sup> Inspired by the Cottrell solute atmosphere model,<sup>[26]</sup> where the drag force depends on the ratio of dislocation velocity,  $v$ , to the diffusivity of the solute atom,  $D_i$  in a function as  $F \propto (v/D_i) \ln(D_i/v)$ , we propose that the additional DSA drag stress can be formulated as  $K_{DSA} \propto (\dot{\epsilon}^m/D_i) \ln(D_i/\dot{\epsilon}^m)$ , which is added to the baseline lattice drag stress. Then the total drag stress is

$$K = K_0 + k_1 T + k_2 \left\langle \frac{\dot{\epsilon}^m}{D_i} \ln \left( \frac{D_i}{\dot{\epsilon}^m} \right) \right\rangle, \quad [26]$$

where  $K_0$ ,  $k_1$ ,  $k_2$  are material constant;  $m$  is a power-law exponent; the function  $\langle \cdot \rangle$  signifies that  $\langle x \rangle = x$ , if  $x > 0$ , and  $\langle x \rangle = 0$ , if  $x < 0$ . Here, the baseline drag stress is formulated as a linear function of temperature, for simplicity. The calibrated Eq. [26] for the mid-life cyclic stress–strain behavior is compared with the

experimental best-fit values, as shown in Figure 8, and it is given in Table II for 1.4848 cast austenitic stainless steel under the tested conditions. It can be inferred from Eq. [26] that either at high temperatures when the diffusion rate of the solute atoms is much larger than the strain rate effect (to the m-power), or at low temperatures when the solute atoms are immobile, the DSA effect would be minimal, since the solute atmosphere would not physically form under these conditions. Therefore, there is no delimitation of the model in this regard. The mid-life hysteresis loops are displaced with the zero points setting at the maximum compression states as shown in Figure 9. The first cyclic stress–strain curve (the curve that connects the peaks of the first-cycle hysteresis loops at different strain ranges), the mid-life cyclic stress–strain curve (the conventional cyclic stress–strain curve), and the last cyclic stress–strain curve (the curve that connects the peaks of the last hysteresis loops at different strain ranges, before load drop due to crack initiation) are also shown to see the evolution of the cyclic stress–strain behavior. At a high strain rate of  $\dot{\epsilon} = 0.02 \text{ s}^{-1}$ , the cyclic stress–strain response curve approaches to the Masing behavior with cyclic hardening (Figure 9(a)). However, at lower strain rates, e.g.,  $\dot{\epsilon} = 0.002 \text{ s}^{-1}$ , the cyclic stress–strain behavior becomes non-Masing due to stronger DSA effect (Figure 9(b)). In essence, DSA is regarded as part of plasticity phenomena, but with a rate-dependent change

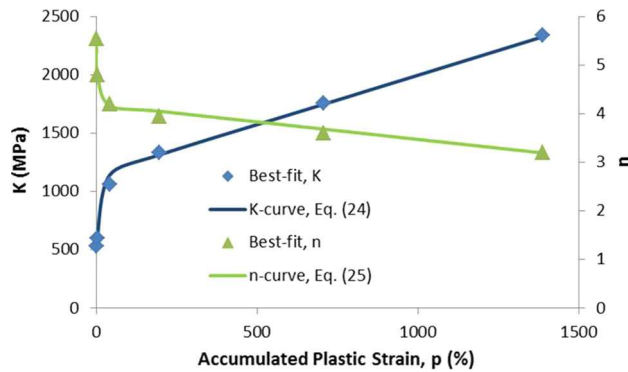


Fig. 7—Plasticity parameters as evolved with accumulated plastic strain for the conditions between  $\pm 0.34$  pct strain at strain rate of  $0.002 \text{ s}^{-1}$ , 673 K (400 °C).

of material microstructure (solute atmosphere and planar slip bands).<sup>[28]</sup> The observed cyclic behavior of 1.4848 cast austenitic stainless steel has negative strain rate sensitivity due to DSA in the intermediate temperature range. Interestingly, in this cast austenitic steel, serrated plastic flow was not observed as in wrought austenitic steels previously studied. This could be due to the difference in the initial dislocation structures of the cast and the wrought materials. In the wrought material, the local high dislocation density may boost the plastic strain rate exceeding the imposed strain rate, thus causing the localized stress relaxation.<sup>[29]</sup> The cyclic behavior at 873 K (600 °C) also exhibits significant cyclic hardening with negative strain rate sensitivity, as shown in Figures 10 and 11. The first, the mid-life and the last cyclic stress–strain curves are also shown for the cyclic stress–strain behaviors at 873 K (600 °C), as shown in Figure 11.

### 3. High temperature behavior [ $>1073 \text{ K}$ (800 °C)]

The cyclic stress behaviors of the material at different strain rates at 1073 K (800 °C) are shown in Figure 12. Even though the initial response appeared to be rate-dependent, after a short number of cycles ( $\sim 100$ ) the material became cyclically stabilized. The mid-life hysteresis loops of the cast austenitic steel at the strain rate of  $\dot{\epsilon} = 0.02$  and  $0.0002 \text{ s}^{-1}$  at this temperature are shown in Figure 13. The strain rate did have an effect on

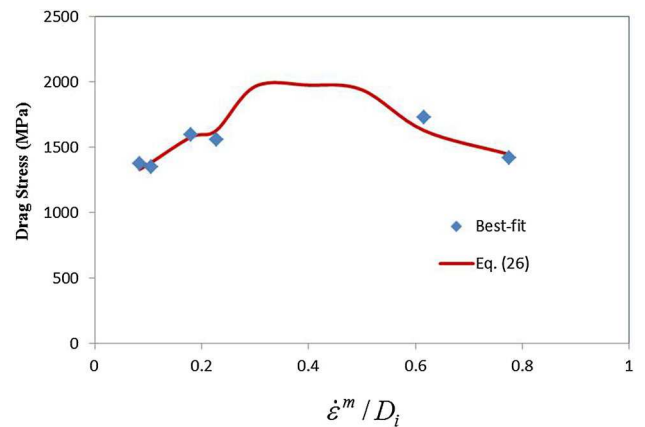


Fig. 8—Drag stress for plasticity considering the effect of DSA.

Table II. Deformation Mechanisms and Parameters

Temperature		293 K (20 °C)	673 K (400 °C)	873 K (600 °C)	1073 K (800 °C)	1173 K (900 °C)
Plasticity	$\sigma_0$ (MPa)	100	100	100	100	70
	$n$	5.54	4.75	4.75	4.75	4.75
	$K$ (MPa)	1217	—	—	—	922
DSA	$K$ (MPa)	$K = 922 + \frac{(1217-922)}{(1173-293)}(1173 - T) + 1800 \left\langle \frac{\dot{\epsilon}^{0.1}}{185 \exp\left(\frac{-30000}{RT}\right)} \ln \left( \frac{185 \exp\left(\frac{-30000}{RT}\right)}{\dot{\epsilon}^{0.1}} \right) \right\rangle$				
Creep	$H$ (MPa)	—	—	—	3734	3734
	$A_0$ ( $\text{s}^{-1}$ )	$1.47 \times 10^{34}$				
	$Q$ (kJ)	891				
	$V$ ( $\text{m}^3$ )	$5.6 \times 10^{-28}$				

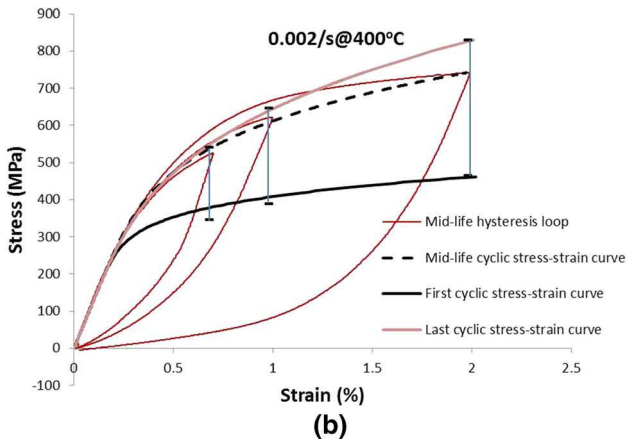
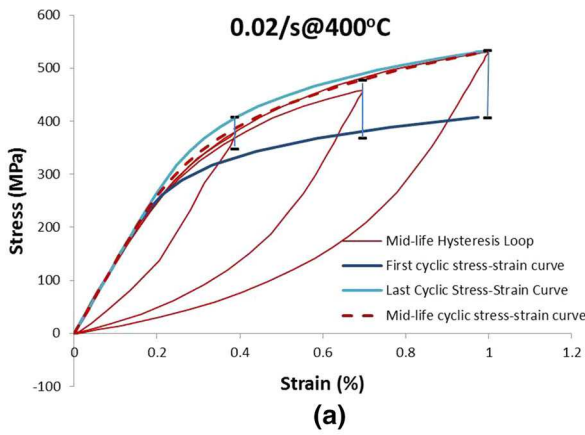


Fig. 9—Mid-life hysteresis behaviors of austenitic cast steel at 673 K (400 °C), (a) at strain rate of  $0.02 \text{ s}^{-1}$ , (b) at strain rate of  $0.002 \text{ s}^{-1}$ .

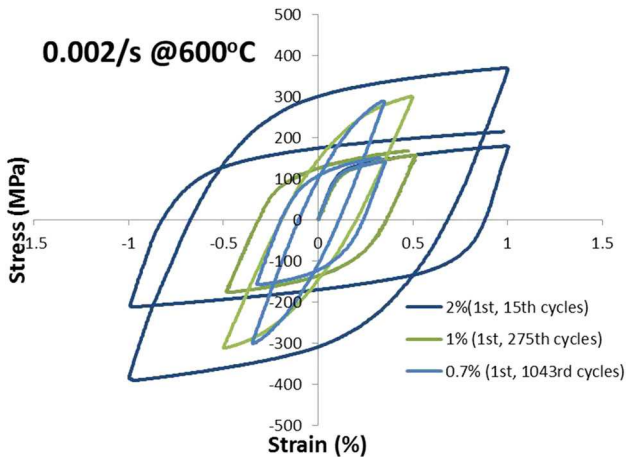


Fig. 10—Hysteresis loops of cast austenitic steel at 873 K (600 °C).

the shape of the hysteresis loop. However, at this temperature, the effect of DSA was balanced by the positive strain rate sensitivity of creep deformation. The cyclic stress-strain behavior of this austenitic steel at 1073 K (800 °C) is highly non-Masing.

At 1173 K (900 °C), the material appeared to be cyclically stable right from the beginning, and it exhibited slightly cyclic-softening, as shown in Figure 14. The positive rate sensitivity was apparent in

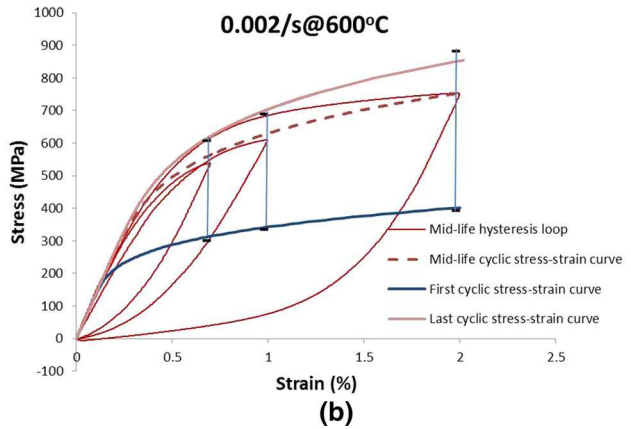
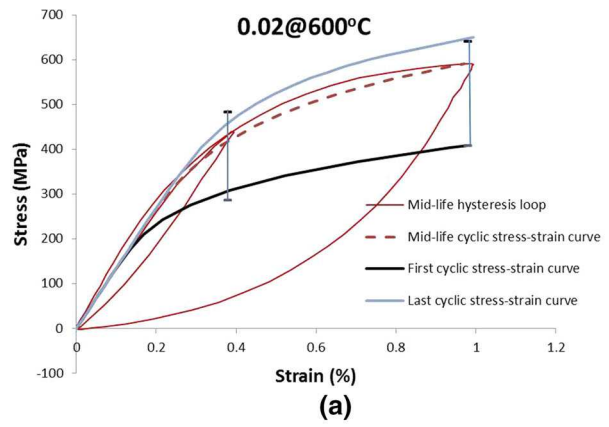


Fig. 11—Mid-life hysteresis behaviors of austenitic cast steel at 600 °C, (a) at strain rate of  $0.02 \text{ s}^{-1}$ , (b) at strain rate of  $0.002 \text{ s}^{-1}$ .

that the slower loading rate caused a significantly lower flow stress behavior. The mid-life hysteresis loops of the material at this temperature are shown in Figures 15(a) and (b), for the two strain rates,  $0.002$  and  $0.0002 \text{ s}^{-1}$ , respectively. The positive strain rate sensitivity should be attributed to operation of time-dependent creep mechanism. The cyclic stress-strain behavior of this austenitic steel at 1173 K (900 °C) appeared to be closely Masing. The slight variations could be due to material variability.

For deformation at 1073 K and 1173 K (800 °C and 900 °C), both plasticity Eq. [2] and creep Eq. [3] are considered in the overall strain formulation Eq. [1], and the descriptions of the cyclic stress-strain behaviors are shown in Figures 13 and 15, respectively. Particularly, it is more evident that at the low strain rate at 1173 K (900 °C), both the cyclic stress-strain and the hysteresis behaviors appear to be governed by dislocation-glide creep as attested by the occurrence of linear work hardening, as formulated in Eq. [10]. Equation [10] also contains a dislocation pile-up recovery term, but its effect is not manifested under the strain-forced test condition. If recovery were significant, it would lead to a non-linear flow stress behavior approaching a constant level (steady-state creep). The effect of recovery can be assessed by switching to constant stress control after pre-loading to a certain deformation level, but such tests were not conducted in the present study. The plasticity

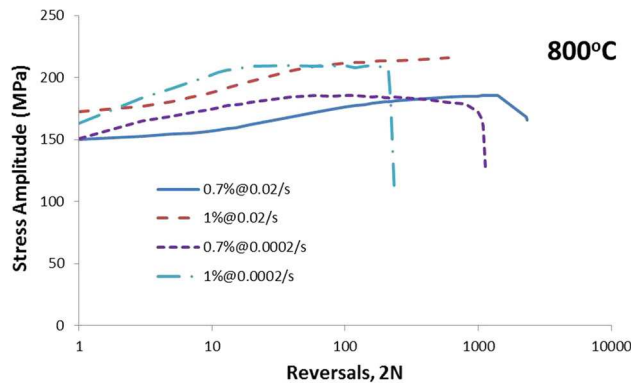


Fig. 12—Cyclic peak-valley stresses of austenitic cast steel at 1073 K (800 °C).

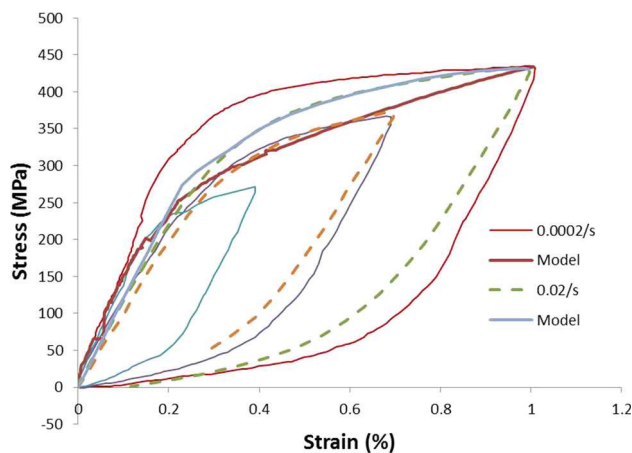


Fig. 13—Mid-life hysteresis behaviors of austenitic cast steel at 1073 K (800 °C).

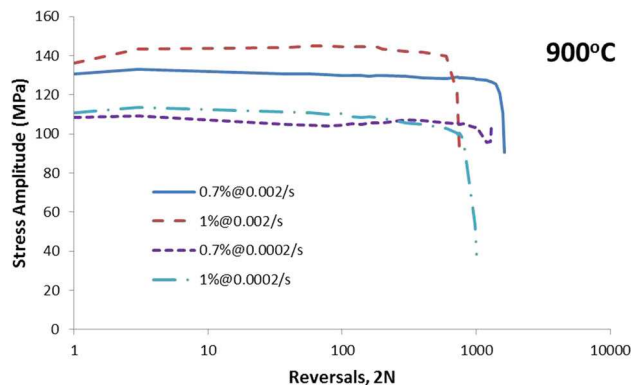
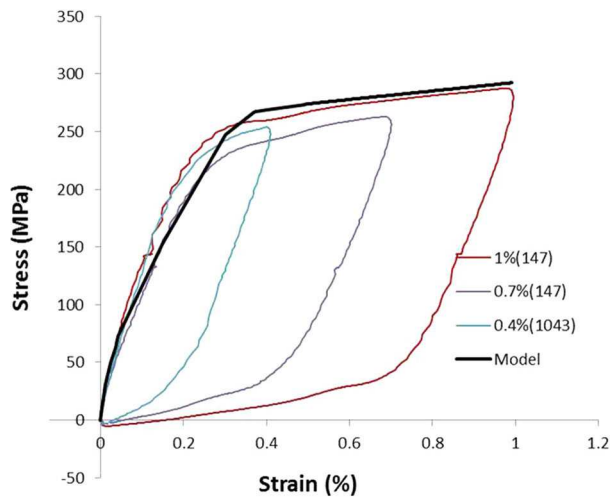
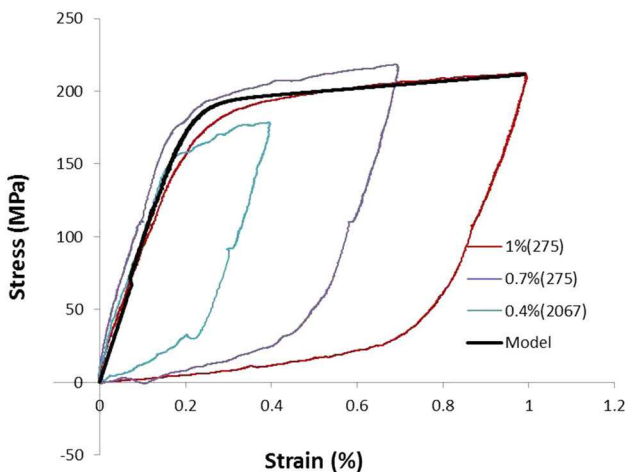


Fig. 14—Cyclic peak-valley stresses of austenitic cast steel at 1173 K (900 °C).

and creep strain accumulation under various test conditions at 1073 K and 1173 K (800 °C and 900 °C) are shown in Figure 16. At 1073 K (800 °C), high strain rate loading still drives plasticity to be dominant, but under low strain rate the contribution of creep rises up, which brings down the DSA hardening effect. At



(a)



(b)

Fig. 15—Mid-life hysteresis behaviors of austenitic cast steel at 1173 K (900 °C), (a) at strain rate of  $0.002 \text{ s}^{-1}$ , (b) at strain rate of  $0.0002 \text{ s}^{-1}$ .

1173 K (900 °C), however, creep deformation becomes predominant with apparent linear strain hardening due to dislocation glide.

In conclusion, the cyclic deformation behavior of 1.4848 cast austenitic steel is well described by the mechanism-based constitutive equation, Eq. [22], which includes rate-independent plasticity and hyperbolic sine creep mechanisms. Even though the viscosity or creep mechanism terms appear in Eq. [22] for low-temperature deformation, but because of the effect of Arrhenius relation governing the creep mechanism(s), it takes a negligible effect, because the material would yield first by rate-independent plasticity mechanism(s). In this regard, there is no delimitation of the present model either, except at very high strain rates when dynamic effects of deformation take place (as the Johnson–Cooke model). The model parameter values for the mid-life cyclic stress–strain curves shown in Figures 4, 9, 11, 13, 15 are given in Table II. It appears that cyclic deformation by pure plasticity is Masing, but when

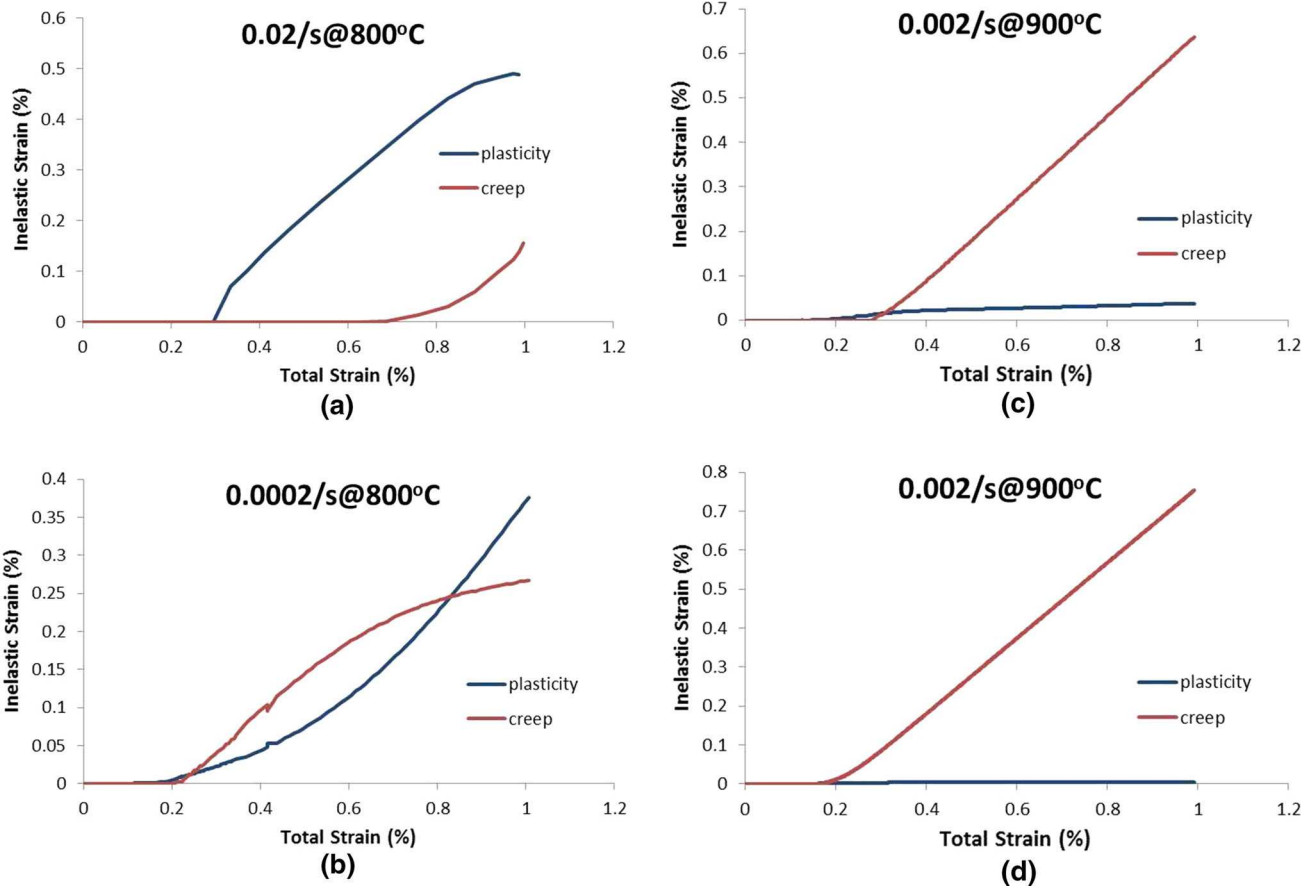


Fig. 16—Plasticity and creep strain accumulation under various test conditions: (a) at  $0.02\text{ s}^{-1}$ , 1073 K (800 °C); (b) at  $0.0002\text{ s}^{-1}$ , 1073 K (800 °C); (c) at  $0.002\text{ s}^{-1}$ , 1173 K (900 °C); and (d) at  $0.0002\text{ s}^{-1}$ , 1173 K (900 °C).

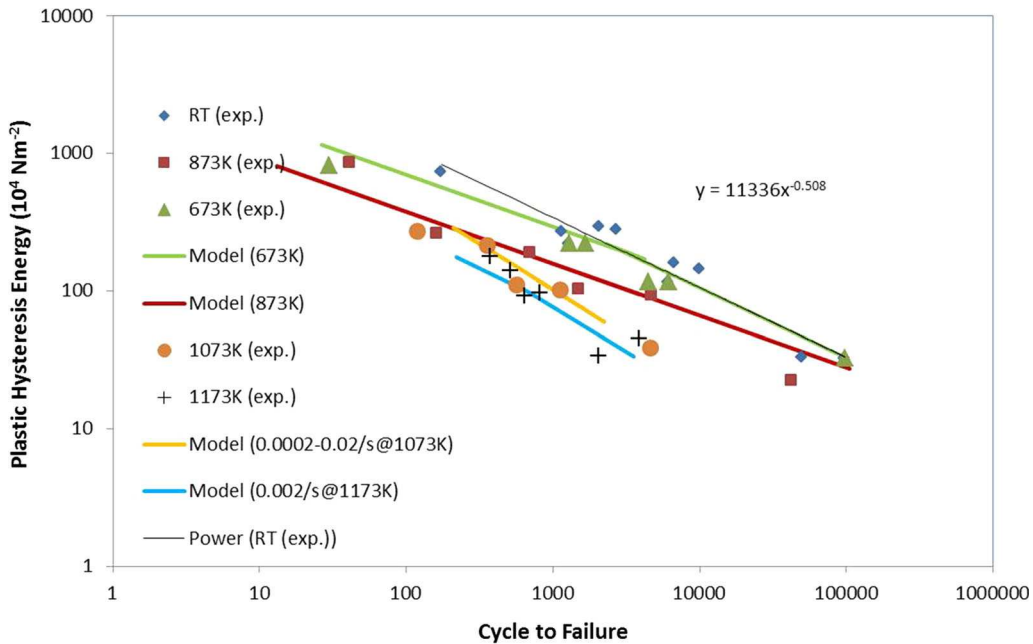


Fig. 17—The inelastic strain range vs fatigue life for 1.4848 stainless steel.

rate-dependent mechanisms intervene the behavior becomes non-Masing. Unified viscoplastic models have been developed for 304L and 316L stainless steels,<sup>[30]</sup> but they do not provide such detailed mechanism delineation.

### B. LCF Life

By the ICFT,<sup>[16–19]</sup> the overall fatigue life consisting of crack nucleation and propagation in coalescence with internally distributed damage can be expressed as

$$\frac{1}{N} = D \left\{ \frac{1}{N_f} + \frac{h}{a_c} \right\}, \quad [27]$$

where  $N_f$  is the pure mechanical fatigue life,  $h$  ( $= \sqrt{2k_{ox}\tau}$ ,  $k_{ox}$  is the oxidation constant,  $\tau$  is the cycle period) is the oxidation increment per cycle,  $a_c$  is the critical crack length at fracture, as given by

$$a_c = \frac{1}{\pi} \left( \frac{K_{IC}}{Y\sigma_{max}} \right)^2 \quad [28]$$

and  $D$  is a factor considering all internally distributed damage/discontinuities, as expressed by

$$D = \left( 1 + \sum_i \frac{l_i}{\lambda_i} \right) \quad [29]$$

where  $l_i$  is the size of the  $i$ -th damage component and  $\lambda_i$  is their interspacing.

Pure mechanical fatigue is regarded as fatigue by cyclic plasticity, usually occurring at RT without contributions of creep and environmental effects. LCF life is

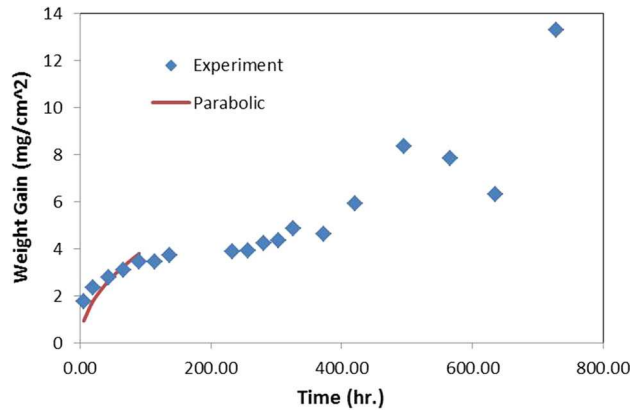


Fig. 18—Oxidation curve of 1.4848 stainless steel at 1173 K (900 °C).

often correlated with the plastic strain range, by the Coffin–Manson relationship, if the material is cyclic stable. For the present case, however, the cast austenitic steel exhibits significant cyclic hardening in the intermediate temperature range, which leads to continuous reduction of plastic strain range during the cycling. Fatigue damage assessment by counting the plastic strain accumulation cycle by cycle would be very tedious in practice. On the other hand, as shown in Figures 3, 5, and 10, the hysteresis energy appears to be fairly constant during the cyclic process, except at very large strains (*e.g.*,  $\Delta\varepsilon = 2$  pct). Therefore, the energy-based Morrow relation seems to be an alternative to characterize fatigue life,<sup>[6]</sup> as

$$W_p = W_0 N_f^d, \quad [30]$$

where  $W_p$  is the plastic strain energy of the hysteresis loop,  $W_0$  and  $d$  are material constants. Since the RT hysteresis loop remains fairly stable, the RT-LCF data are used to calibrate Eq. [30] for pure mechanical fatigue, as shown in Figure 17.

At intermediate temperatures, 673 K and 873 K (400 °C and 600 °C), DSA promotes slip inhomogeneity with dislocation pile-ups, forming concentrated slip bands or dislocation walls. For example, a planar slip structure of DSA was observed in 316L stainless steel.<sup>[28]</sup> Imagining dislocation pile-ups are embryos of cracks, the internal damage by DSA can be formulated as proportional to the excess forest dislocation density. Therefore, the  $D$ -factor for austenitic stainless steel can be written as

$$D = 1 + \alpha \left[ \left( \frac{\Delta\sigma_H}{\mu b} \right)^2 - \rho_0 \right] + \beta \varepsilon_v, \quad [31]$$

where  $\Delta\sigma_H$  is the amplitude of cyclic hardening (maximum attainable peak stress minus the peak stress of the first cycle),  $\rho_0$  is the dislocation density level below which there is no instantaneous crack nucleation, and  $\alpha$  the proportional constant for dislocation-nucleated cracks, and  $\beta$  is proportional constant for creep damage.

It is seen in Figures 9 and 11 that the DSA effect is more pronounced at higher strain amplitudes and lower strain rates at 673 K to 873 K (400 °C to 600 °C), and hence this would result in an increased  $D$ -factor by Eq. [31], given that the creep strain at these intermediate temperatures is minimal. As shown in Figure 17, the LCF life at 673 K to 873 K (400 °C to 600 °C) is indeed significantly reduced at high strain amplitudes, as compared to the RT baseline. As temperature increases to 1073 K and 1173 K (800 °C and 900 °C), the DSA term in Eq. [31] becomes negligible or have no effect at

Table III. Life Prediction Parameter

Mechanism Parameter (unit)	Fatigue		DSA		Creep $\beta$	Oxidation: $k_{ox} = k_0 \exp(-Q/RT)$		
	$W_{p10}$ ( $10^4$ N m <sup>-2</sup> )	$d$	$\alpha$ (m <sup>2</sup> )	$\rho_0$ (m <sup>-2</sup> )		$k_0$ (m <sup>2</sup> /s)	$Q$ (kJ)	$K_{IC}/Y$ (MPa√m)
Value	11,336	-0.508	$0.228 \times 10^{-12}$	$3.71 \times 10^{12}$	1200	1.7	231	32

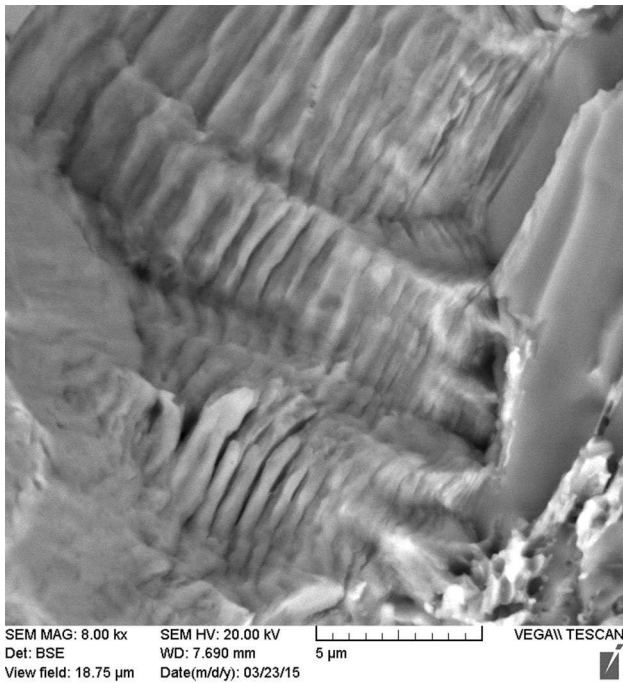


Fig. 19—Striations on room-temperature fatigue fracture specimen with 0.7 pct strain range.

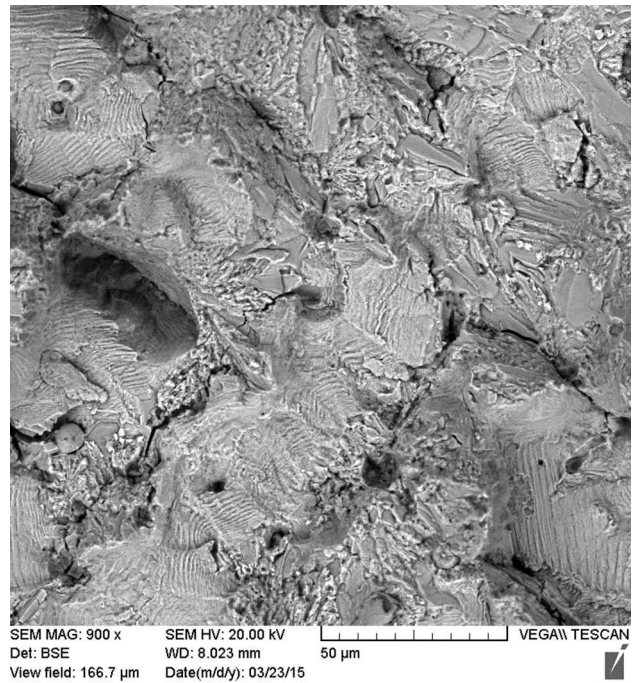


Fig. 21—Fracture surface of specimen fatigued with 0.7 pct strain range at  $0.002 \text{ s}^{-1}$ , 873 K (600 °C).

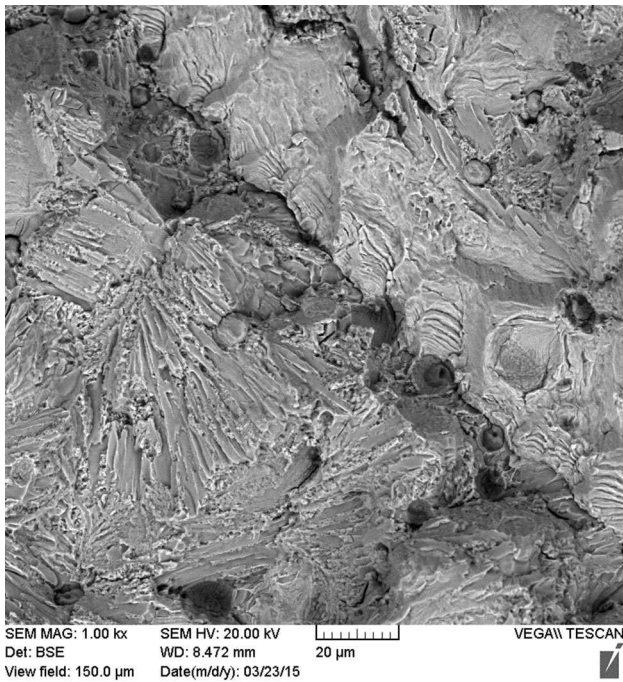


Fig. 20—Fracture surface of specimen fatigued with 0.7 pct strain range at  $0.002 \text{ s}^{-1}$ , 673 K (400 °C).

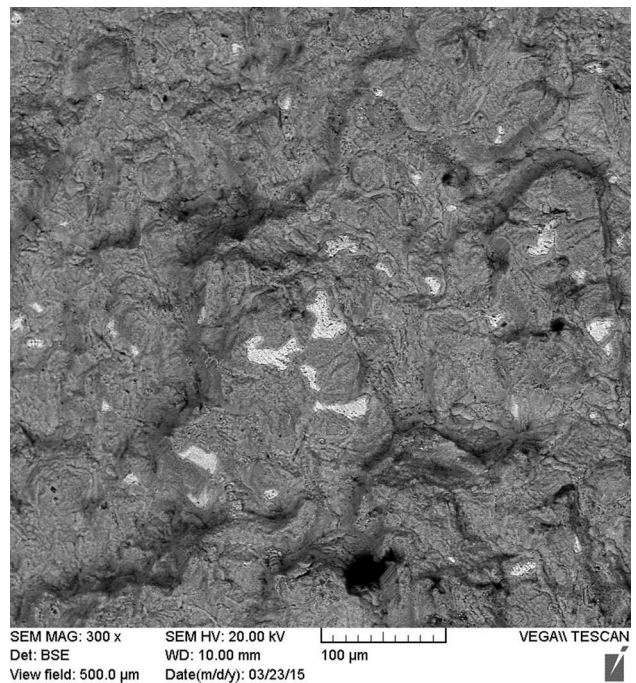


Fig. 22—Fracture surface of specimen fatigued with 0.7 pct strain range at  $0.002 \text{ s}^{-1}$ , 1073 K (800 °C). The white spots are areas of high Ni content.

all, since the cyclic hardening is balanced by the creep softening, but the creep damage term remains in Eq. [31].

In addition to mechanical fatigue and creep, at high temperatures, oxidation plays an important role. The oxidation curve of 1.4848 austenitic stainless steel at 1173 K (900 °C) is shown in Figure 18. The parabolic

law constant is calibrated to the curve. As shown in Figure 18, the combination of creep and oxidation does reduce the LCF life significantly in comparison with the RT-LCF life where the above effects are absent.

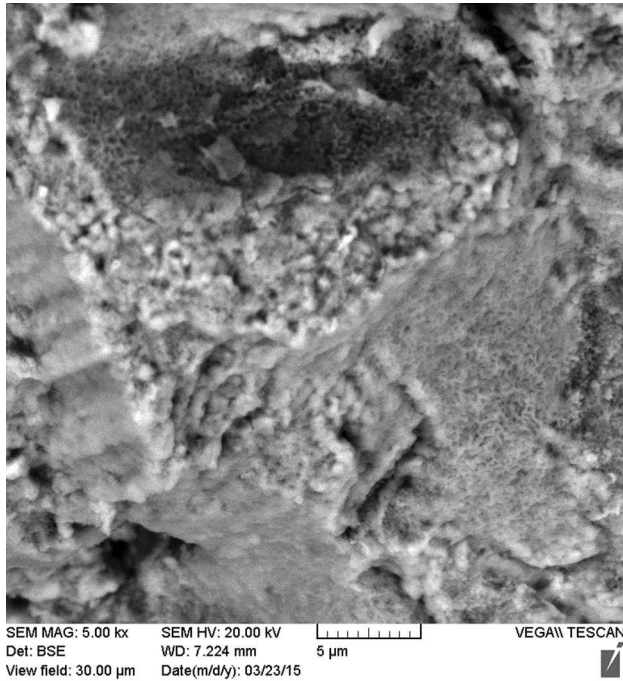


Fig. 23—Fracture surface of specimen fatigued with 0.7 pct strain range at  $0.002 \text{ s}^{-1}$ , 1173 K (900 °C).

Considering all the above mechanisms and effects, the model predictions are shown (as lines) in comparison with the experimental data. The model parameters for life prediction are given in Table III. As indicated by Eq. [27], the interaction between creep and oxidation is non-linear. Creep deformation on one hand reduces the LCF life by a factor of  $D$  as expressed by Eq. [31], but on the other hand, it lowers the peak stress, which allows the specimen to tolerate a longer crack, thus increasing the crack propagation life. Similarly, lowering the controlling strain rate allows more creep deformation to relax the peak stress, but it also allows more time of oxidation per cycle. All such conflicting effects result in a rather frequency-insensitive behavior of LCF life of 1.4848 steel at high temperature (see Figure 17), which is also reflected in the model curves for 1073 K and 1173 K (800 °C and 900 °C) at different strain rates.

Seifert *et al.* used a crack-tip plastic blunting model to describe the LCF and TMF behavior of 1.4849 steel.<sup>[31]</sup> Their model, however, does not separate the mechanisms of plasticity and creep, nor does it consider oxidation explicitly. The ICFT model quantitatively delineates the effects of the above mechanisms, so that they can be tailored in material design to yield the optimum performance.

### C. Fractographic Observation

Using SEM, it was observed that the RT fracture surface contained typical striations that indicate transgranular fatigue fracture as shown in Figure 19. Fatigue fracture at 673 K to 873 K (400 °C to 600 °C) was also transgranular, however, DSA led to a concentrated slip-band pattern, as shown in Figures 20 and 21. At

1073 K (800 °C), the fatigue specimen failed predominantly by an intergranular fracture mode, as shown in Figure 22. On the fracture surface of the specimen failed at 1173 K (900 °C), extensive oxidation and formation of voids or cavities can be observed, as shown in Figure 23. The above metallurgical evidence supports that creep has a significant effect on fracture at 1073 K to 1173 K (800 °C to 900 °C). These fractographic observations corroborate with the model descriptions.

## V. CONCLUSION

The mechanism-based constitutive model is developed within the framework of ICFT for 1.4848 austenitic stainless steel. As a limiting case, the ICFT model predicated that deformation and fatigue at low temperature are controlled by plasticity. At the intermediate temperatures, 673 K to 873 K (400 °C to 600 °C), due to the effect of DSA which increases the drag stress of plasticity, the material cyclic hardens continuously until failure. The model attributes the reduction of fatigue life to the internal damage related to the excess dislocation density caused by slip concentration. At high temperatures, 1073 K and 1173 K (800 °C and 900 °C), both creep and oxidation come into play, the ICFT specifically delineates the effects of the two mechanisms in a non-linear combination, which is expressed as the ratio of the oxidation penetration to the critically tolerable crack length,  $h/a_c$ . The onset of creep at high temperature would reduce the flow stress and hence reducing the  $h/a_c$  ratio, which means increase the LCF life, but at the same time creep physically creates internal damage that would knockdown the fatigue life by a factor of  $D$ , as in Eq. [31]. The model descriptions of the cyclic stress–strain behavior, LCF life, and fracture modes all agree very well with the experimental observation and post-mortem fractographic examinations on 1.4848 austenitic stainless steel. Therefore, the model is able to faithfully capture the underlying deformation/damage mechanisms and quantify contribution from each mechanism. The understanding can be used in material/component design to optimize the performance.

## ACKNOWLEDGMENTS

The material testing that was carried out as a contract between the National Research Council of Canada and Westcast Industries Inc is gratefully acknowledged. This work is partially supported by the Program of Energy Research and Development (PERD), Natural Resources Canada. Ryan MacNeil, Technical Officer of National Research Council Canada, is thanked for his assistance in material testing.

## REFERENCES

1. A.H. Cottrell: *Philos. Mag.*, 1953, vol. 44, p. 829.
2. R. Alain, P. Violan, and J. Mendez: *Mater. Sci. Eng. A*, 1997, vol. 229A, pp. 87–94.

3. S.-G. Hong, S.-B. Lee, and T.-S. Byun: *Mater. Sci. Eng. A*, 2007, vol. 457A, pp. 139–47.
4. Y.-J. Kim, H. Jang, and Y.-J. Oh: *Mater. Sci. Eng. A*, 2009, vol. 526A, pp. 244–49.
5. L.F. Coffin, Jr: *ASME Trans.*, 1954, vol. 76, p. 931.
6. J.D. Morrow: Cyclic plastic strain energy and fatigue of metals, *Internal Friction, Damping and Cyclic Plasticity, ASTM STP*, 1965, vol. 378, pp. 45–84.
7. J.L. Chaboche: *Int. J. Plast.*, 2008, vol. 24, pp. 1642–93.
8. E. Orowan: *Proc. R. Soc. Lond. A*, 1939, vol. 171A, pp. 79–105.
9. N. Thompson and J.J. Wadsworth: *Adv. Phys.*, 1958, vol. 7, pp. 72–169.
10. H. Mughrabi: in *The Strength of Metals and Alloys*, vol. 3, P. Haasen, V. Gerold, and G. Kostorz, eds., Pergamon Press, Oxford, 1980, pp. 1615–39.
11. B.-T. Ma and C. Laird: *Acta Metall.*, 1989, vol. 37, pp. 337–48.
12. J. Weertman: *J. Appl. Phys.*, 1955, vol. 26, pp. 1213–17.
13. H.J. Frost, M.F. Ashby: *Deformation Mechanism Maps*, Pergamon Press, Oxford, 1982.
14. A.J. Perry: *J. Mater. Sci.*, 1974, vol. 9, pp. 1016–39.
15. M.E. Kassner and T.A. Hayes: *Int. J. Plast.*, 2003, vol. 19, pp. 1715–48.
16. X.J. Wu, G. Quan, R. MacNeil, Z. Zhang, C. Sloss, *Metall. Mater. Trans. A*, 2014, vol. 45A, pp. 5088–97.
17. X.J. Wu, G. Quan, R. MacNeil, Z. Zhang, X. Liu, C. Sloss, *Metall. Mater. Trans. A*, 2015, vol. 46A, pp. 2530–43.
18. X.J. Wu: *Key Eng. Mater.*, 2015, vol. 627, pp. 341–44.
19. X.J. Wu: *ASME J. Gas Turbine Powers*, 2009, vol. 131, pp. 032101/1–6.
20. X.J. Wu and A.K. Krausz: *J. Mater. Eng. Perform.*, 1994, vol. 3, pp. 169–77.
21. J.P. Hirth, J. Lothe: *Theory of Dislocation*, Krieger Publishing Company, Malabar, 1992.
22. A.S. Krausz and H. Eyring: *Deformation Kinetics*, Wiley, New York, 1975.
23. W. Prager: *Proc. 8th Int. Congr. Appl. Mech., Istanbul*, 1952, vol. 2, p. 65.
24. X.J. Wu, Z. Zhang, L. Jiang, and P. Patnaik: *J. Eng. Gas Turbines Power*, 2017, vol. 139, pp. 052101/1–5.
25. S.-G. Hong, K.-O. Lee, J.-Y. Lim, and S.-B. Lee: *Key Eng. Mater.*, 2005, vols. 297–300, pp. 2477–82.
26. C. Fressengeas, A.J. Beaudoin, M. Lebyodkin, L.P. Kubin, and Y. Estrin: *Mater. Sci. Eng. A*, 2005, vol. 400–401A, pp. 226–30.
27. A.K. Miller (ed.): *Unified Constitutive Equations for Plastic Deformation and Creep of Engineering Alloys*, Elsevier Applied Science Publishers, London, 1987, pp. 138–215.
28. S.-G. Hong and S.-B. Lee: *J. Nucl. Mater.*, 2005, vol. 340, pp. 307–14.
29. P. Rodriguez: *Bull. Mater. Sci.*, 1984, vol. 6 (4), pp. 653–63.
30. L. Taleb, G. Cailletaud, and K. Saï: *Int. J. Plast.*, 2014, vol. 61, pp. 32–48.
31. T. Seifert, C. Schweizer, M. Schlesinger, M. Moser, and M. Eibl: *Int. J. Mater. Res.*, 2010, vol. 101 (8), pp. 942–50.